# Photo-induced desorption of NO from NiO(100): calculation of the four-dimensional potential energy surfaces and systematic wave packet studies†

**Imed Mehdaoui,‡[a] Dominik Kröner,‡[b] Mikhail Pykavy,‡[c] H.-J. Freund[d] and Thorsten Klüner*[e]**

*Received 9th September 2005, Accepted 18th October 2005*
*First published as an Advance Article on the web 16th November 2005*
**DOI: 10.1039/b512778e**

The velocity distributions of the laser-induced desorption of NO molecules from an epitaxially grown film of NiO(100) on Ni(100) have been studied [Mull *et al*., *J. Chem. Phys*., 1992, **96**, 7108]. A pronounced bimodality of velocity distributions has been found, where the NO molecules desorbing with higher velocities exhibit a coupling to the rotational quantum states *J*. In this article we present simulations of state resolved velocity distributions on a full *ab initio* level. As a basis for this quantum mechanical treatment a 4D potential energy surface (PES) was constructed for the electronic ground and a representative excited state, using a $NiO_5Mg_{13}^{18+}$ cluster. The PESs of the electronic ground and an excited state were calculated at the CASPT2 and the configuration interaction (CI) level of theory, respectively. Multi-dimensional quantum wave packet simulations on these two surfaces were performed for different sets of degrees of freedom. Our key finding is that at least a 3D wave packet simulation, in which the desorption coordinate $Z$, polar angle $\theta$ and lateral coordinate $X$ are included, is necessary to allow the simulation of experimental velocity distributions. Analysis of the wave packet dynamics demonstrates that essentially the lateral coordinate, which was neglected in previous studies [Klüner *et al*., *Phys. Rev. Lett*. 1998, **80**, 5208], is responsible for the experimentally observed bimodality. An extensive analysis shows that the bimodality is due to a bifurcation of the wave packet on the excited state PES, where the motion of the molecule parallel to the surface plays a decisive role.

## 1. Introduction

The understanding of simple photochemical reactions on surfaces can provide insight into complex phenomena such as photocatalysis, atmospheric chemistry and solar energy conversion. However, a detailed mechanistic study of surface photochemistry necessitates a significant reduction of complexity with respect to the reaction under investigation. In this respect, laser-induced desorption of small molecules from surfaces is a well studied phenomenon as it represents the simplest surface photochemical reaction.[1–4] Despite its apparent simplicity, basic mechanistic questions are still controversial. In particular, the origin of bimodal velocity distributions occurring in UV laser-induced desorption experiments of NO from NiO(100) (*cf*. Fig. 1) has been the subject of detailed theoretical investigations in recent years.[5–7] In fact, a bifurcation of a wave packet on a 2D excited state *ab initio* PES was proposed to be the origin of this bimodality as revealed by stochastic quantum dynamical studies.[5] However, no pronounced bimodality was found in a recent semi-classical study in which the 2D *ab initio* PES was empirically extended up to seven degrees of freedom. Additionally, a late desorption channel was obtained which could not be observed in earlier studies due to limited simulation time.[6,7]

In contrast to this, we will demonstrate in the present study that a bifurcation of a wave packet on the excited state PES is in fact the mechanistic origin of the aforementioned bimodality. Our study is based on high quality *ab initio* PESs for the ground and excited electronic states involved in the desorption process. These PESs were constructed by considering four degrees of freedom. The model and the construction of the PESs will be presented in section 2. Section 3.1 discusses the methods used for the simulation. The results of the subsequent stochastic wave packet calculations, which are presented in section 3.2, 3.3 and 3.4, provide a detailed picture of the nuclear dynamics of the desorption process and reveal the limited accuracy of empirical PES. Section 4 concludes this article.

[a] *Carl von Ossietzky Universität Oldenburg, Institut für Reine und Angewandte Chemie, Postfach 2503, D-26111 Oldenburg, Germany*
[b] *Universität Potsdam, Theoretische Chemie, Karl-Liebknecht-Str. 24-25, D-14476 Potsdam-Golm, Germany*
[c] *Technische Universität Berlin, Institut für Chemie, Straße des 17. Juni 135, D-10623 Berlin, Germany*
[d] *Fritz-Haber-Institut der Max-Planck-Gesellschaft, Faradayweg 4-6, D-14195 Berlin, Germany*
[e] *Carl von Ossietzky Universität Oldenburg, Institut für Reine und Angewandte Chemie, Postfach 2503, D-26111 Oldenburg, Germany. E-mail: Thorsten.Kluener@uni-oldenburg.de*
† This work is dedicated to Prof. Dr Volker Staemmler on the occasion of his 65th birthday.
‡ Also at Fritz-Haber-Institut der Max-Planck-Gesellschaft, Faradayweg 4-6, D-14195 Berlin, Germany.

 

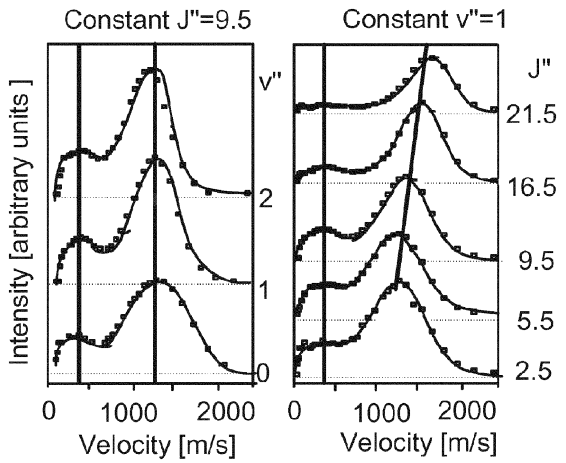


**Fig. 1** Experimental velocity distributions of vibrationally ($v''$) and rotationally ($J''$) excited NO molecules after laser-induced desorption from NiO(100), obtained from resonance enhanced multiphoton ionisation (REMPI) spectroscopy.[4] For a given $J''$ (left side) a decoupling of translation and vibration is found, while for a given $v''$ (right side) a coupling of rotation and translation is observed for molecules desorbing with high velocities (fast channel).

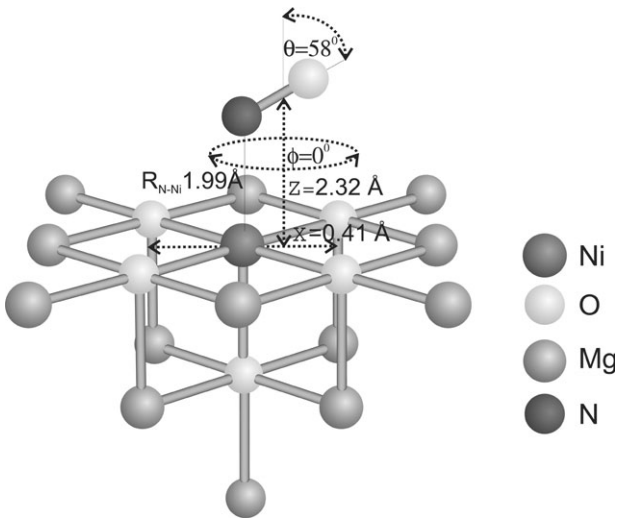


**Fig. 2** Minimum energy geometry of NO on the $NiO_5Mg_{13}^{18+}$ cluster in the ground state. The PCF used is not shown.

## 2. Potential energy surfaces

### 2.1. Model and method of calculation

To represent the NiO(100) surface, a $NiO_5Mg_{13}^{18+}$ cluster, embedded in a Madelung field of 2906 point charges, was used. The point charge field (PCF) was constructed with point charges of $\pm 2e$ and simulates the long range Coulomb interaction between the crystal bulk and the adsorbate system. The geometry of the $NiO_5Mg_{13}^{18+}$ cluster was adapted from the ideal rock salt structure of bulk NiO with a lattice constant of 4.18 Å.[8]

While the $NiO_5Mg_{13}^{18+}$ cluster was assumed to be rigid, four degrees of freedom of the NO molecule were considered in our simulations, *cf*. Fig. 2: (i) the desorption coordinate $Z$, *i.e*. the distance between the NiO surface and the center of mass of NO; (ii) the lateral coordinate $X$, describing the motion of the center of mass of the NO molecule along the Ni–Ni surface diagonal; (iii) the polar angle $\theta$ between the NO bond and the surface normal (for $\theta = 0^\circ$ the NO bond is perpendicular to the surface with the N atom on top of the surface); and (iv) the azimuthal angle $\phi$ between the NO bond and the Ni–Ni surface line (for $\phi = 0^\circ$ and $\theta = 90^\circ$ the NO bond is in-line with the Ni–Ni line). Note that in the present study the polar angle $\theta$ is defined differently from that in ref. 5 where a change in the polar tilt angle $\alpha$ was combined with a change in the center of mass of the NO molecule.

Because the NO vibration has been found to be decoupled from translation (see Fig. 1), the NO bond length was fixed at the value $R_{NO} = 1.170$ Å which corresponds to the adsorption minimum and agrees well with previous theoretical calculations.[9]

The electronic ground state of $NO/NiO_5Mg_{13}^{18+}$ is a doublet state[10] technically derived from antiferromagnetic coupling of two unpaired 3d Ni electrons in the cluster with the single unpaired electron of the NO molecule. To construct an appropriate molecular orbital space the complete active space self-consistent field (CASSCF) method was used.[11,12] The (3,3) active space consists of the $3d(z^2)$ and $3d(x^2-y^2)$ orbitals of Ni and the NO $2\pi^*(z)$ antibonding orbital and contains three electrons (see for instance active orbitals for the adsorption minimum, Fig. 3). In addition, dynamic electron correlation effects were treated perturbatively by means of CASPT2 calculations.[13,14]

Note that in our $NiO_5Mg_{13}^{18+}$ cluster model all but the central Ni atom were approximated by Mg atoms. In order to test the validity of the PES along the lateral coordinate $X$ calculations with a larger cluster containing two Ni atoms were carried out. Fig. 4 shows the ground state potential along $X$ for the $NiO_5Mg_{13}^{18+}$ and the $Ni_2O_8Mg_{18}^{24+}$ model. Since the two potential energy curves are in good agreement for all $X$ this result justifies the use of the $NiO_5Mg_{13}^{18+}$ model for the calculation of the PESs for the electronic ground and excited states along all four degrees of freedom.

A number of electronic excited states might be involved in the DIET (desorption induced by electronic transition) process, possibly at the same time.[10] In the present study only the energetically lowest charge transfer state, with one electron transferred from the cluster to the $2\pi^*$ orbitals of the NO molecule resulting in an $NO^-(NiO^+)$-like intermediate,[15] was considered. Furthermore, only ferromagnetic coupling of three unpaired electrons in the cluster and two unpaired

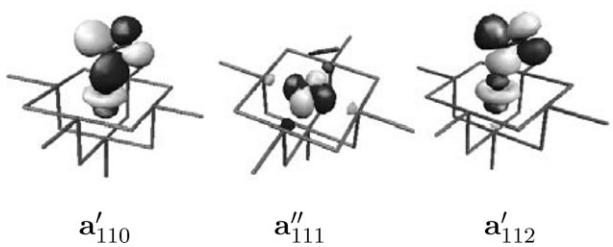


**Fig. 3** Active molecular orbitals of the $NO–NiO_5Mg_{13}^{18+}$ PCF from CASSCF(3,3) for the adsorption minimum in the ground state.

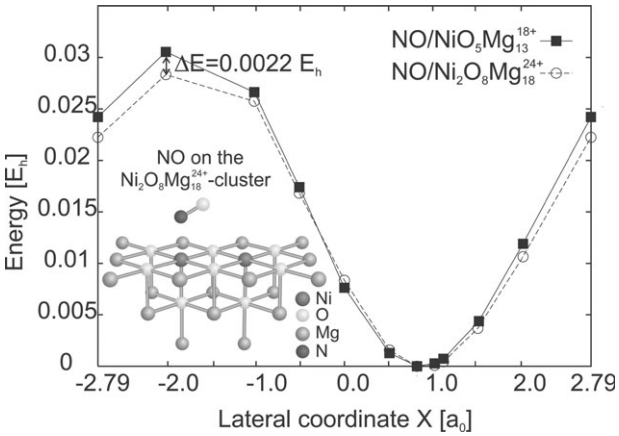


**Fig. 4** Ground state PES of NO on the $NiO_5Mg_{13}^{18+}$ (filled squares) and $Ni_2O_8Mg_{18}^{24+}$ cluster (circles) for $Z = 2.32$ Å, $\phi = 0°$ and $\theta = 58°$. The inset shows NO on the $Ni_2O_8Mg_{18}^{24+}$ cluster.

electrons in the $NO^-$ anion was considered, giving rise to a sextet state. Previous studies imply that the consideration of only one representative excited state is a reasonable approximation due to the topological similarity of various charge transfer states of the NO–NiO(100) system.[10]

To optimize the occupied molecular orbitals for the chosen charge transfer state a modification of the conventional SCF scheme was needed which is not suitable to obtain an appropriate description of the NO anion at the technically positively charged cluster. For this reason the 3s Ni orbital obtained for the electronic ground state had its occupation fixed to one and was frozen so as to allow all other orbitals to relax. The electronic excited state was then derived by means of the valence configuration interaction (VCI) method with the active space consisting of 16 oxygen 2sp orbitals in the top most cluster layer and the 3d orbitals of Ni, and a valence space of NO (3σ, 4σ, 5σ, 1π and 2π*orbitals). In addition only those electronic configurations were allowed which exactly correspond to the proposed charge transfer scheme, *i.e.* the oxygen orbitals of the cluster disgorge one electron which is added to the valence space of the NO molecule. In this way a wave function was obtained for the technically highly excited electronic state according to the intended physical nature of this state but without any further restrictions (like for instance the locality of the electron hole in the cluster).

The basis sets used were at least of triple-ζ quality (see Table 1 for details). Augmenting diffuse and polarization functions were chosen in such a way as to ensure that all important interaction components are properly covered by the applied quantum chemical methods, whilst keeping computational costs maintainable. All CASSCF/CASPT2 calculations for the electronic ground state were performed using the MOLCAS 5.4 package.[16] Results for the excited (charge transfer) state were obtained using the Bochum suite of *ab initio* programs.[17–20]

### 2.2. Calculated potential energy surfaces

In the minimum energy geometry of the electronic ground state the N atom of the NO molecule is located on top of the $Ni^{2+}$ cation with a N–Ni bonding distance of 1.99 Å. The NO molecule is tilted by $\theta = 58°$ from the surface normal and is in-line with the Ni–Ni line of the NiO surface ($\phi = 0°$), see Fig. 2.

**Table 1** Basis sets used for the quantum chemical calculations

| Atom type Standard basis | Extentions Ground state | Excited state |
|---|---|---|
| Ni, Wachters (14s9p5d) → ⟨9s6p4d⟩ | +s(ζ = 0.35) +p(ζ = 0.25) +d(ζ = 0.15) +2 × f(ζ = 2.1; 0.7) | +s(ζ = 0.35) |
| O (Cluster), Huzinaga (9s5p) → ⟨6s3p⟩ | +s,p(ζ = 0.1; 0.1) +d(ζ = 0.4)[a] | +s,p(ζ = 0.1; 0.1) |
| Mg | (10s6p) → ⟨2s1p⟩[b] | Pseudo-potentials (Stoll) |
| N, Huzinaga (9s5p) → ⟨6s3p⟩ | +s(ζ = 0.0576) +p(ζ = 0.0491) +3 × d(ζ = 0.9; 0.3; 0.1) +f(ζ = 0.3) | +s(ζ = 0.0576) +p(ζ = 0.0491) +2 × d(ζ = 1.654; 0.469) |
| O(NO), Huzinaga (9s5p) → ⟨6s3p⟩ | +s(ζ = 0.0738) +p(ζ = 0.0597) +3 × d(ζ = 1.2; 0.4; 0.15) +f(ζ = 0.4) | +s(ζ = 0.0738) +p(ζ = 0.0597) +2 × d(ζ = 2.314; 0.645) |

[a] For the oxygen ions in the uppermost surface layer only. [b] Exponents and contraction coefficients optimized for $Mg^{2+}$.

These *ab initio* results agree with recent experimental values of $\theta = 59°$ [21] for the bonding angle and $1.88 \pm 0.02$ Å[21,22] for the N–Ni length. For the minimum energy geometry a counterpoise corrected[23] NO cluster adsorption energy of −0.34 eV[24] was obtained at CASPT2 level which underestimates the experimental bond strength of $-0.57 \pm 0.04$ eV[25] due to the limited cluster size, the finite one-particle basis and the approximate treatment of electron correlation. For a detailed discussion on the effect of the basis functions and cluster size on the adsorption energy the reader is referred to ref. 9.

On the excited state PES the energetic minimum is located at a smaller NO surface distance ($Z = 2.12$ Å) than the minimum of the ground state potential ($Z = 2.32$ Å). Furthermore, the $NO^-$ species in the excited state prefers an almost horizontal position on the surface ($\theta = 88°$), where the O atom of the NO is pointing towards the central Ni atom ($\phi = 0°$) and the center of mass of NO is shifted along the lateral coordinate near the central point of the Ni–Ni surface diagonal ($X = -1.32$ Å).

These findings complement previous studies, in which the lateral translation coordinate $X$ and the azimuthal angle $\phi$ had been neglected.[5] The fact that the energetic minimum of the excited state PES lies at a shorter $Z$ than in the ground state PES would lead to an Antoniewicz-like[26] desorption mechanism in the case of a 1D model (*i.e.* $V(Z)$), but due to the high dimensionality of the actual PES the mechanism turns out to be more complex.

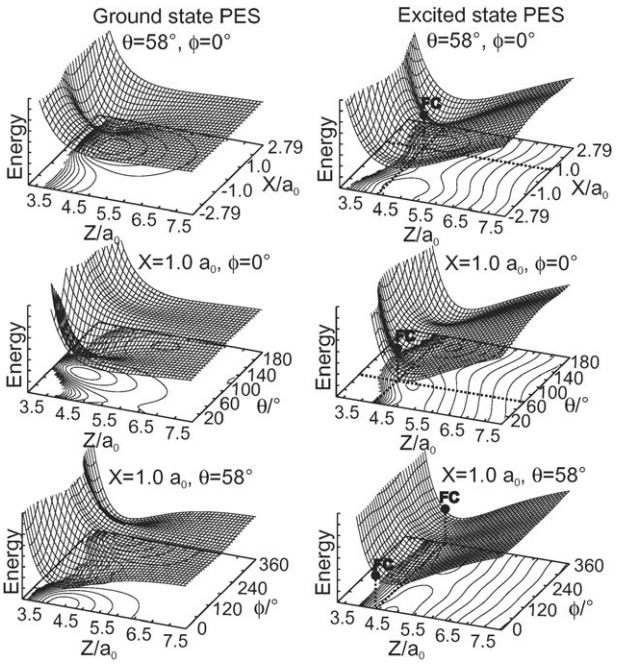


**Fig. 5** 2D cuts of the 4D PESs for the electronic ground state (left) and an excited state (right). FC indicates the Franck–Condon point.

### 2.3. Fit functions

More than 4000 energy data points were obtained from single-point calculations for the ground state along the four coordinates $Z$, $X$, $\theta$ and $\phi$. Almost twice as many data points were produced to represent the excited state. Using these *ab initio* data 3D PESs were constructed using the following analytical expression:

$$V_{\mathrm{g,e}}(Z,\theta,\kappa) = \sum_{i=1}^{m_i} f_1 f_2 (e_1 + e_2)\left(\frac{\alpha}{Z^2}+1\right) - \frac{\beta}{Z} + \gamma,$$

where

$$f_1(\theta) = \sum_{l=0}^{m_l} a_{il}(\cos^l[\theta - a'_{il}] + a''_{il}),$$

$$f_2(\kappa) = \sum_{l=0}^{m_l} b_{il}(\cos^l[\kappa - b'_{il}] + b''_{il}),$$

$$e_1(Z) = \sum_{j=1}^{m_j} g_{ij}\exp[g'_{ij}(Z - g''_{ij})],$$

$$e_2(Z) = \sum_{j=1}^{m_j} h_{ij}\exp[h'_{ij}(Z - h''_{ij})]^2, \qquad (2.1)$$

with $\kappa$ being either $\phi$ or $X$. $V_{\mathrm{g}}$ and $V_{\mathrm{e}}$ represent the electronic ground and an excited state, respectively.

The parameters $\alpha$, $\beta$, $\gamma$, $a_{il}$, $a'_{il}$, $a''_{il}$, $b_{il}$, $b'_{il}$, $b''_{il}$, $g_{ij}$, $g'_{ij}$, $g''_{ij}$, $h_{ij}$, $h'_{ij}$, $h_{ij}''$ have been fitted to the calculated energy data points by means of the standard Levenberg–Marquardt algorithm.[27] 2D cuts of the 4D PES for the ground and electronic excited state are shown in Fig. 5.

The geometrical parameters for the energetic minimum of the ground and excited state PES are collected in Table 2.

**Table 2** Geometrical parameters for the minimum energy configuration of the ground and an excited state on fitted PESs

| Fit coordinates | $Z$/Å | $\theta$/° | $\phi$/° | $X$/Å |
|---|---|---|---|---|
| Ground state | | | | |
| $Z$, $\theta$, $\phi$ | 2.28 | 60 | 0 | 0.54 (fixed) |
| $Z$, $\theta$, $X$ | 2.28 | 66 | 0 (fixed) | 0.58 |
| Excited state | | | | |
| $Z$, $\theta$, $\phi$ | 2.33 | 114 | 180 | 0.54 (fixed) |
| $Z$, $\theta$, $X$ | 2.17 | 99 | 0 (fixed) | −1.32 |

## 3. Quantum dynamics

### 3.1. Propagation method

The nuclear dynamics on the PESs of the electronic ground (g) and excited (e) state were simulated by multi-dimensional wave packet calculations on the basis of the time-dependent Schrödinger equation

$$i\frac{\partial \Psi_{\mathrm{g,e}}(Z,\theta,\phi,X,t)}{\partial t} = \hat{H}_{\mathrm{g,e}}(Z,\theta,\phi,X)\Psi_{\mathrm{g,e}}(Z,\theta,\phi,X,t). \qquad (3.2)$$

The molecular Hamiltonian $\hat{H}_{\mathrm{g,e}}$ of the NO molecule is given by

$$\hat{H}_{\mathrm{g,e}}(Z,\theta,\phi,X) = -\frac{1}{2\mu R_{\mathrm{NO}}^2}\left(\frac{1}{\sin\theta}\frac{\partial}{\partial\theta}\sin\theta\frac{\partial}{\partial\theta} + \frac{1}{\sin^2}\frac{\partial^2}{\partial\phi^2}\right) - \left(\frac{1}{2M}\right)\left(\frac{\partial^2}{\partial Z^2}\right) - \left(\frac{1}{2M}\right)\left(\frac{\partial^2}{\partial X^2}\right) + V_{\mathrm{g,e}}(Z,\theta,\phi,X), \qquad (3.3)$$

with the total mass $M$, the reduced mass $\mu$ and the bond distance $R_{\mathrm{NO}}$ of the NO molecule. In our quantum dynamical simulations the time evolution operator was approximated by the second order split-operator method by Feit and Fleck[28] using time steps of 10 or 50 $\hbar/E_{\mathrm{h}}$ for propagation on the excited and ground state potential, respectively. In order to check the numerical results of the observables of interest the Chebychev propagator[29] was used as an accurate reference. The initial state of our simulations was the energetically lowest rovibrational eigenfunction $\Psi_0$ of the electronic ground state PES. To model the substrate mediated excitation of the NO–NiO system $\Psi_0$ was transferred vertically onto the excited state potential where it was propagated for specific residence times $\tau_n$. The desorption process was simulated by a vertical transfer of the wave packet back onto the ground state potential, where it was propagated until a final time $t_f$. Here a final propagation time of $t_f$ = 10 ps was sufficient to ensure convergence for asymptotic observables of each quantum trajectory. The part of the wave packet in the far asymptotic region of the ground state potential corresponds to desorbed NO molecules. State resolved velocity distributions were obtained from momentum space probability densities in the asymptotic region for each rotational state $J$. This analysis was done by separating the wave packet in the asymptotic

region by multiplying it by a smooth transfer function

$$f_{\text{trans}} = \frac{1}{1 + \exp[a(Z - Z_0)]} \tag{3.4}$$

according to the grid change technique of Heather and Metiu.[30] In order to describe an ensemble of molecules in a dissipative scenario the incoherent average scheme for different residence times $\tau_n$ of $N$ quantum trajectories proposed by Gadzuk[31] was applied. In this method, the expectation values or distributions of desired observables

$$A(t;\tau_n) = \langle \Psi_{\text{des}}(t;\tau_n) | \hat{A} | \Psi_{\text{des}}(t;\tau_n) \rangle \tag{3.5}$$

are averaged with an exponential factor using the following equation:

$$A(t;\tau) = \frac{\sum_{n=1}^{N} A(t;\tau_n) \exp\left(-\frac{\tau_n}{\tau}\right)}{\sum_{n=1}^{N} \exp\left(-\frac{\tau_n}{\tau}\right)}. \tag{3.6}$$

Here $\Psi_{\text{des}}$ denotes the desorbed part of the wave packet which is located in the asymptotic region. The resonance time $\tau$ is the only empirical parameter. A resonance lifetime $\tau$ of 48.4 fs (2000 $\hbar/E_{\text{h}}$) has been used resulting in desorption probabilities comparable to experimental findings.[32] This jumping wave packet scenario is the simplest way to treat electronic relaxation which turns out to be a coupling of the adsorbate–substrate system to a bath of electron–hole pairs within the framework of dissipative quantum dynamics. Convergence of the Gadzuk averaging was obtained for $N = 83$ quantum trajectories, *i.e.* residence times of $\tau_n = (120 + 120i)\hbar/E_{\text{h}}$ with $i = 0,1,2,\ldots,N-1$. The parameters for the wave packet propagations are given in Table 3.

### 3.2. Excited state dynamics

Fig. 6 shows the expectation values of the desorption coordinate $\langle Z \rangle$, the lateral coordinate $\langle X \rangle$, the polar angle $\langle \theta \rangle$ and the azimuthal angle $\langle \phi \rangle$ as a function of the residence time $\tau_n$ for the wave packet evolving on the excited state potential. Two 2D wave packet simulations, including $Z$ and either $\theta$ or $X$, and two 3D wave packet simulations, including $Z$, $\theta$, and either $X$ or $\phi$, were considered.

Fig. 6a presents the expectation value of the desorption coordinate $\langle Z \rangle$. Even though the energetic minimum of the excited state potential is located at a shorter $Z$ than the minimum of the ground state, in all four wave packet simulations the expectation value $\langle Z \rangle$ of the desorption coordinate initially increases until a residence time of $\tau_n \approx 85$ fs.

This initial increase in $\langle Z \rangle$ can be understood by looking at the Franck–Condon points in the 2D cuts of the excited state potential, see Fig. 5. The topology of the excited state PES in the region of $Z > 5.2\ a_0$ forces the wave packet to eventually move back towards the surface for $\tau_n > 100$ fs. Here, a more pronounced decrease in $\langle Z \rangle$ is observed for the wave packet simulations which included the lateral coordinate $X$ (3D($Z$, $\theta$, $X$) and 2D($Z$, $X$)). Since the lateral coordinate $X$ is of major importance for the bimodal characteristics in the velocity distribution, as will be shown in section 3.3, this means that the laser excitation leads to a pronounced motion of the NO molecule along the desorption coordinate in the electronically excited state. As can be seen from the wave packet simulations (excluding $X$) with and without the azimuthal angle $\phi$ (3D($Z$, $\theta$, $\phi$) and 2D($Z$, $\theta$)) the omission of $\phi$ has only little influence on the expectation value $\langle Z \rangle$. This is due to the weak $\phi$ gradients, *cf.* Fig. 5. Thus, $\phi$ should be of minor importance and we would also expect to find a pronounced oscillation in $\langle Z \rangle$ in the case of a 4D treatment including $Z$, $\theta$, $X$ and $\phi$.

Fig. 6b illustrates the expectation value of the lateral coordinate $X$. In the range of $0 < \tau_n < 50$ fs the change in $\langle X \rangle$ is about 0.8 $a_0$. This strong dynamics clearly points to the importance of this coordinate. Furthermore, the polar angle $\theta$ has only a small influence on $\langle X \rangle$.

**Table 3** Numerical parameters used in the quantum wave packet studies

| Constants | | |
|---|---|---|
| Mass of NO molecule | $M$ | 54 697.7686 $m_{\text{e}}$ |
| Moment of inertia of NO molecule | $I$ | 66 552.9811 $m_{\text{e}}a_0{}^2$ |
| Reduced mass of NO molecule | $\mu$ | 13 614.1342 $m_{\text{e}}$ |
| Internal N–O distance | $r_0$ | 2.21 $a_0$ |
| *Z*-Grid | | |
| Start | $Z_{\min}$ | 3.0 $a_0$ |
| End | $Z_{\max}$ | 16.0 $a_0$ |
| Number of grid points | $N_Z$ | 256 |
| Grid spacing | $\Delta Z$ | 0.051 $a_0$ |
| Maximum momentum | $k_{\text{zmax}}$ | 61.6 $\hbar/a_0$ |
| Momentum resolution | $\Delta kZ$ | 0.48 $\hbar/a_0$ |
| Grid change | | |
| Center of transfer function | $Z_0$ | 13.5 $a_0$ |
| Width of transfer function | $a$ | 6.0 $a_0$ |
| Grid start | $Z2_{\min}$ | 11.16 $a_0$ |
| Grid end | $Z2_{\max}$ | 17.63 $a_0$ |
| Grid points | $N2_Z$ | 128 |
| Grid spacing | $\Delta Z_2$ | 0.051 $a_0$ |
| Maximum momentum | $k2_{\text{zmax}}$ | 61.62 $\hbar/a_0$ |
| Momentum resolution | $\Delta kZ_2$ | 0.96 $\hbar/a_0$ |
| *X*-Grid | | |
| Start | $X_{\min}$ | −2.789 95 $a_0$ |
| End | $X_{\max}$ | 2.789 95 $a_0$ |
| Number of grid points | $N_{\text{X}}$ | 128 |
| Grid spacing | $\Delta X$ | 0.044 $a_0$ |
| Maximum momentum | $k_{\text{xmax}}$ | 71.5 $\hbar/a_0$ |
| Momentum resolution | $\Delta kX$ | 1.117 $\hbar/a_0$ |
| $\theta$-Grid | | |
| Start | $\theta_{\min}$ | 0° |
| End | $\theta_{\max}$ | 180° |
| Number of grid points | $N_\theta$ | 80 |
| Maximum rotational state | $J_{\max}$ | 79 |
| $\phi$-Grid | | |
| Start | $\phi_{\min}$ | 0° |
| End | $\phi_{\max}$ | 360° |
| Number of grid points | $N_\theta$ | 159 |
| Maximum rotational state | $J_{\max}$ | 79 |
| Propagation | | |
| Time step (excited state) | $\Delta t$ | 10 $\hbar/E_{\text{h}}$ |
| Time step (ground state) | $\Delta t$ | 50 $\hbar/E_{\text{h}}$ |
| Spacing of excited state Lifetime grid | $\Delta\tau_n$ | 120 $\hbar/E_{\text{h}}$ |
| Number of quantum trajectories | $N$ | 83 |
| Total propagation time | $t$ | 400 000 $\hbar/E_{\text{h}}$ |

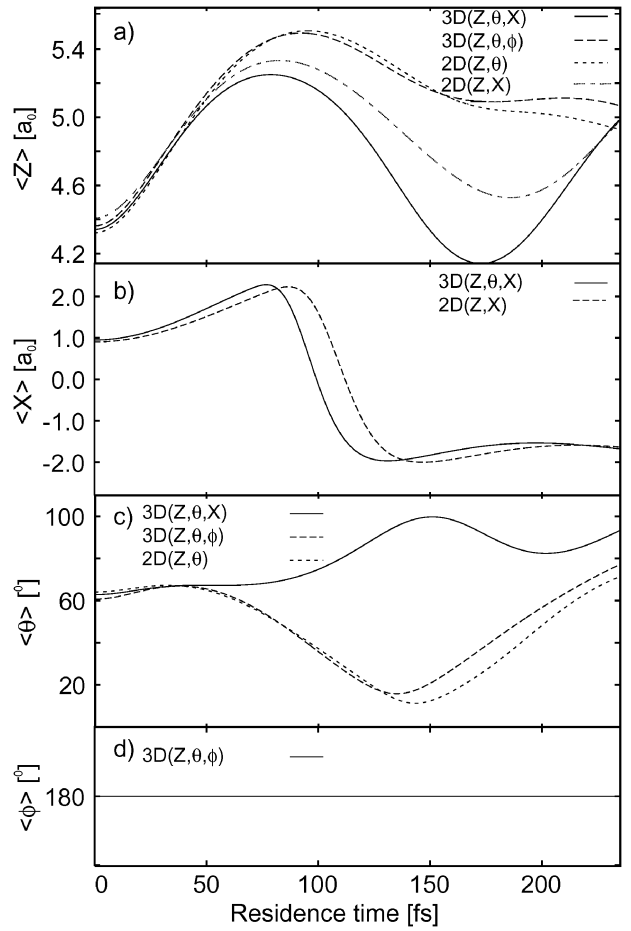


**Fig. 6** Expectation values of the rovibrational ground state wave packet $\Psi_0$ evolving on the electronically excited state PES. The insets show the expectation values of (a) the desorption coordinate $Z$, (b) the lateral coordinate $X$, (c) the polar angle $\theta$ and (d) the azimuthal angle $\phi$.

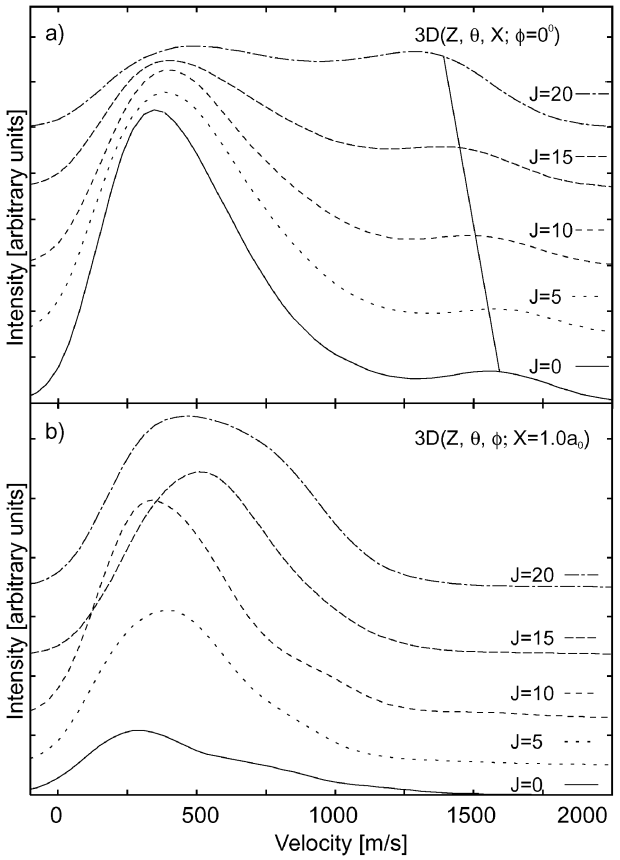


**Fig. 7** Averaged velocity distributions for a resonance lifetime $\tau$ = 48.4 fs (2000 $\hbar/E_h$) and rotational quantum states $J$ = 0, 5, 10, 15, 20. (a) The 3D($Z$, $\theta$, $X$) study exhibits bimodal velocity distributions in which the fast desorption channel is coupled to the rotational quantum states $J$ as indicated by the solid line (adapted from ref. 24). (b) In the 3D($Z$, $\theta$, $\phi$) study no bimodal characteristics can be observed in the velocity distributions.

Inspection of Fig. 6c reveals that the wave packet simulations show different characteristics in the expectation value of the polar angle $\langle\theta\rangle$ depending on the inclusion of the lateral coordinate $X$. By excluding $X$ from the simulation, $\langle\theta\rangle$ decreases until $\tau_n \approx 150$ fs, whereas in the 3D($Z$, $\theta$, $X$) case $\langle\theta\rangle$ increases and then starts to oscillate around $\langle\theta\rangle \approx 90°$, which means that the NO molecule prefers an almost horizontal position on the excited state PES. This is in contrast to previous studies from Klüner *et al.*[5] in which the lateral coordinate has been omitted. The azimuthal angle $\phi$ has only a small effect on the dynamics as can be seen from the 2D($Z$, $\theta$) and 3D($Z$, $\theta$, $\phi$) studies.

As both PESs involved in the desorption process are symmetric with respect to the azimuthal angle $\phi = 180°$, the expectation value $\langle\phi\rangle$ remains constant during the simulation, see Fig. 6d.

### 3.3. Velocity distributions

The lifetime averaged velocity distributions for selected rotational quantum numbers $J$ are presented in Fig. 7a and Fig. 7b for the 3D($Z$, $\theta$, $X$) and 3D($Z$, $\theta$, $\phi$) study, respectively, using a representative resonance lifetime of $\tau$ = 48.4 fs (2000 $\hbar/E_h$). Pronounced bimodal characteristics in the velocity distributions are observed if the lateral coordinate $X$ is included in the 3D wave packet studies.[24] If the lateral coordinate $X$ is not accounted for, the final velocity distributions exhibit only one rather unstructured peak in the range of 0–1200 m s$^{-1}$, see Fig. 7b. Inclusion of $X$ yields a pronounced bimodality with a slow desorption channel at about 300–400 m s$^{-1}$ and a fast desorption channel at 1300–1600 m s$^{-1}$. This is in good agreement with the experimental velocity distributions (Fig. 1), in which a slow desorption channel is observed in the range of about 200–500 m s$^{-1}$ and a fast desorption channel in the range of about 1200–1600 m s$^{-1}$.[4,33]

Two discrepancies can be observed between the experimental results and our theoretical calculations. First, the coupling between the fast desorption channel and the rotational quantum states $J$ and second the correlation between the rotational quantum states $J$ and the intensities of the fast and slow desorption channel are reversed. In a former study [5] the correct coupling between the rotational quantum states $J$ and the fast desorption channel was found. This is possibly due to a cancellation of errors, since only two degrees of

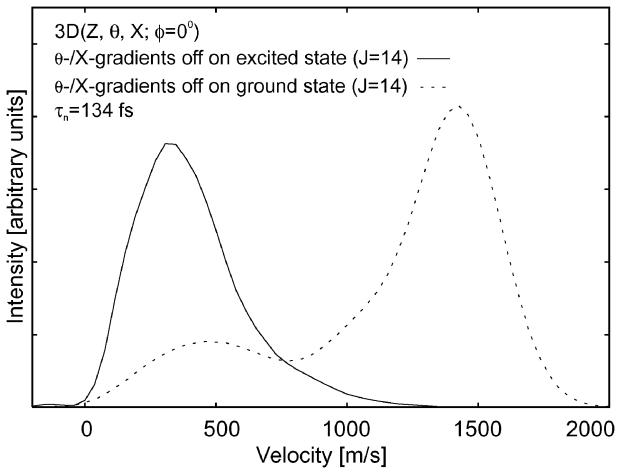


**Fig. 8** Final velocity distributions for a representative residence time $\tau_n = 134$ fs (5520 $\hbar/E_h$) for the rotational quantum state $J = 14$ after turning off the $\theta$ and $X$ gradients in the excited state (solid line) or ground state (dashed line) PES (adapted from ref. 24).

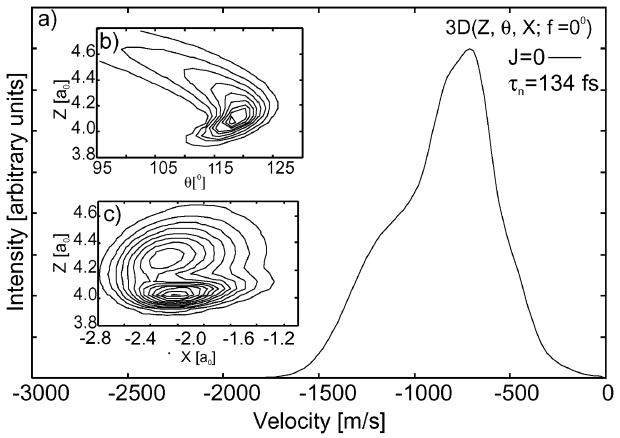


**Fig. 9** (a) Velocity distribution of the wave packet on the excited state PES for a specific residence time $\tau_n = 134$ fs (5520 $\hbar/E_h$) and rotational quantum number $J = 0$. Insets (b) and (c) show 2D contour plots of the wave packet on the excited state PES after a residence time $\tau_n = 134$ fs.

freedom, *i.e.* the desorption coordinate $Z$ and the polar angle $\theta$, were considered. In the present study the incorrect coupling of rotation and translation may be due to the omission of other degrees of freedom, such as the azimuthal angle $\phi$, which contributes to the rotational quantum state. The effect of the azimuthal angle $\phi$ on the distinctive features of the velocity distributions is currently investigated in 4D studies and should give insight into the origin of the discussed problems.

To elucidate the origin of bimodal velocity distributions we performed additional calculations in which the gradients of either the excited or ground state potential are set to zero for both the lateral coordinate $X$ and polar angle $\theta$. As an example, a characteristic quantum trajectory, with a residence time of $\tau_n = 134$ fs, is considered. These calculations show that a bimodal distribution is only observed if the $X$ and $\theta$ gradients of the excited state PES are non-zero with a slow and a fast desorption channel being in the same velocity range as in the full treatment, see dashed line in Fig. 8. Evidently, the dynamics on the excited state PES is responsible for the observed bimodality.

In order to improve our understanding on the microscopic scale, an extensive analysis of the time evolution of the initial wave packet on the excited state PES was performed. Two 2D contour plots of this wave packet and the velocity distribution at $\tau_n = 134$ fs are shown in Fig. 9. As can be seen in Fig. 9a, after a residence time of $\tau_n = 134$ fs, the wave packet in the excited state is moving towards the surface and the velocity distribution exhibits bimodal characteristics. Close examination of the 2D contour plots of the wave packet in Fig. 9b and c proves that the wave packet is divided at $Z \approx 4.15\ a_0$ into two partial wave packets separated by the lateral coordinate $X$. This is caused by the topology of the excited state PES leading to two pathways for the wave packet. Because the two partial wave packets differ in their surface distance $Z$ they will result in a bimodal velocity distribution after relaxation to the ground state and dissociation. This is, of course, only valid if the ground state PES has very little or no influence on the shape of the wave packet in momentum space after relaxation as can be deduced from results presented in Fig. 8. Note that the velocity distribution of the chosen quantum trajectory with a residence time of $\tau_n = 134$ fs is weighted in the Gadzuk averaging by approximately the same amount as the velocity distribution for $\tau_n = 48.4$ fs (resonance lifetime $\tau = 48.4$ fs) due to the increase in the desorption yield for $\tau_n > 100$ fs, see Fig. 10 and the discussion in section 3.4.

Naturally, the choice of the resonance lifetime, which is the only empirical parameter in our calculation, has an influence on the bimodal characteristics of the 3D($Z$, $\theta$, $X$) wave packet study. For resonance lifetimes of less than 24 fs (1000 $\hbar/E_h$) no bimodality can be observed, whereas the velocity distributions exhibit only one channel in the same range as the slow desorption channel with the resonance lifetime $\tau = 48.4$ fs. With resonance lifetimes of greater than 24 fs the fast desorption channel at 1300–1600 m s$^{-1}$ appears. The intensity of this peak in the velocity distributions increases for longer resonance lifetimes. Thus, a realistic resonance lifetime of the wave packet on the excited state PES can be assessed to be

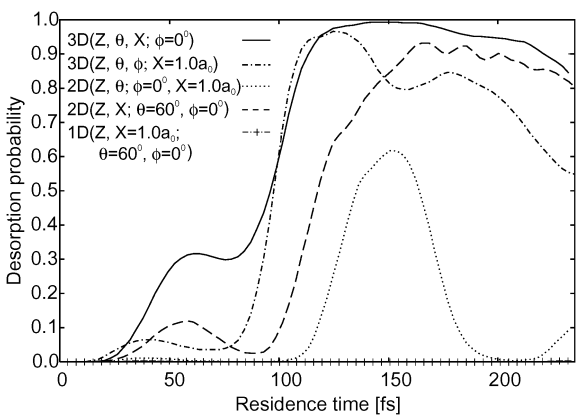


**Fig. 10** Desorption probability as a function of the residence time for the three-dimensional 3D($Z$, $\theta$, $X$) (solid line) and 3D($Z$, $\theta$, $\phi$) (dot-dashed line), the 2D($Z$, $\theta$) (dotted line), 2D($Z$, $X$) (dashed line) and 1D($Z$) (crossed line) wave packet study.

greater than 24 fs, which is in agreement with previous studies.[5] Indeed, the chosen resonance lifetime of $\tau = 48.4$ fs for our wave packet simulations could still be underestimated.

### 3.4. Desorption probability

The desorption probability per excitation event is calculated as the square norm of the desorbing part of the wave packet $\Psi_{\mathrm{des}}$

$$P_{\mathrm{des}}(t;\tau_n) = \langle \Psi_{\mathrm{des}}(t;\tau_n) | \Psi_{\mathrm{des}}(t;\tau_n) \rangle \qquad (3.7)$$

Fig. 10 shows the desorption probability as a function of the residence time $\tau_n$ for the discussed two 3D wave packet simulations, two 2D wave packet simulations including the desorption coordinate $Z$ and either the polar angle $\theta$ or the lateral coordinate $X$ and a 1D simulation in which only the desorption coordinate $Z$ was included.

After keeping all of the coordinates except the desorption coordinate $Z$ fixed to the minimum energy configuration the desorption probability (crossed line in Fig. 10) is close to zero for all residence times $\tau_n$ (*e.g.* $P_{\mathrm{des}}(50\ \mathrm{fs}) = 10^{-3}$). Thus a 1D treatment is not sufficient to describe the desorption process in the NO–NiO(100) system. If $Z$ and $\theta$ are considered in the simulations (dotted line), almost no desorption occurs for residence times $\tau_n = 0$–100 fs which are relevant for the incoherent averaging scheme. Noticeable desorption is found only for residence times greater than 100 fs. However, a remarkable increase of the desorption probability is observed in the 2D studies if the lateral coordinate $X$ is included (dashed line) instead of the polar angle $\theta$. In this case, the desorption probability shows one small peak at $\tau_n \approx 60$ fs followed by a strong increase of the desorption probability for $\tau_n > 100$ fs. This again proves the importance of the lateral coordinate $X$. The 3D($Z$, $\theta$, $\phi$) simulation (dot-dashed line) shows similar characteristics, whereas the first peak at $\tau_n \approx 40$ fs is more pronounced and is followed by a strong increase at $\tau_n \approx 80$ fs. Finally, the 3D($Z$, $\theta$, $X$) simulation (solid line) results in a high desorption probability peak at $\tau_n \approx 60$ fs followed by an increase to almost 1.0 for $\tau_n > 90$ fs. Since the gradients in the azimuthal angle $\phi$ are weak, we expect that a further increase of dimensionality to four dimensions will only slightly change the observed results for the 3D($Z$, $\theta$, $X$) simulation (see also discussion in section 3.2).

## 4. Conclusions

The theoretical quantitative and qualitative descriptions of the bonding of NO on a NiO(100) surface and the corresponding bond breaking during photodesorption of NO represents a challenge to theory. In this study the system was treated systematically from one to three dimensions on an *ab initio* basis. For the photodesorption a two state model was applied using the electronic ground state and a representative electronic excited state, where one electron is transferred from the cluster to the NO molecule, resulting in an $NO^-$–$NiO^+$ intermediate. It has been shown that a 1D treatment, where only the desorption coordinate $Z$ is considered, does not lead to a successful desorption. Including the lateral coordinate $X$ results in a drastic increase in the desorption yield, since this coordinate couples strongly to the other degrees of freedom. However, a 2D treatment of the photodesorption process is still not sufficient to describe the bimodal characteristics of the experimentally observed velocity distributions.

Reasonable agreement with the experimental results and our theoretical calculations could be obtained by a 3D wave packet study including the desorption coordinate $Z$, the lateral coordinate $X$ and the polar angle $\theta$. The main experimental features, *i.e.* the bimodal characteristics of the velocity distributions being calculated in the correct velocity range, could be reproduced. For these simulations a resonance lifetime of $\tau = 48.4$ fs for the $NO^-$–$NiO^+$ intermediate was successfully applied. In contrast to Bach *et al.*[6,7] no "late" desorption channel was observed in our calculations even though each quantum trajectory was propagated until its desorption yield converged ($t_f = 10$ ps). This clearly indicates the necessity of using *ab initio* PESs in the simulation of laser-induced desorption of NO from a NiO(100) surface. Two discrepancies from experiments have been observed: (1) the intensities of the two desorption channels are reversed and (2) the velocity of the fast desorption channel decreases with increasing $J$. These discrepancies have to be addressed in further experimental and theoretical investigations.

New physical insight into mechanisms at the microscopic level has been obtained by identifying the origin of the bimodality in the velocity distributions to be a splitting of the wave packet in the lateral coordinate $X$ on the electronically excited state PES into "fast" and "slow" parts.

For future investigations we will further increase the dimensionality of the quantum dynamical calculations to four dimensions. Also, the explicit treatment of the experimental laser excitation in combination with dissipative quantum dynamics is currently under investigation, which should provide even more information.

We gratefully acknowledge financial support by the Deutsche Forschungsgemeinschaft (SPP1093) and thank Dr S. Borowski for many valuable discussions.

## References

1 S. Borowski, T. Klüner and H.-J. Freund, *J. Chem. Phys.*, 2003, **119**, 10367.
2 H. Guo, P. Saalfrank and T. Seideman, *Prog. Surf. Sci.*, 1999, **62**, 239.
3 S. Thiel, M. Pykavy, T. Klüner, H.-J. Freund, R. Kosloff and V. Staemmler, *Phys. Rev. Lett.*, 2001, **87**, 077601.
4 T. Mull, B. Baumeister, M. Menges, H.-J. Freund, D. Weide, C. Fischer and P. Andresen, *J. Chem. Phys.*, 1992, **96**, 7108.
5 T. Klüner, H.-J. Freund, V. Staemmler and R. Kosloff, *Phys. Rev. Lett.*, 1998, **80**, 5208.
6 C. Bach, T. Klüner and A. Groß, *Chem. Phys. Lett.*, 2003, **376**, 424.
7 C. Bach, T. Klüner and A. Groß, *Appl. Phys. A*, 2004, **78**, 231.
8 R. W. G. Wyckoff, *Crystal Structures* , John Wiley & Sons, New York, 2nd edn, 1964.
9 G. Pacchioni, C. D. Valentin, D. Dominguez-Ariza, F. Illas, T. Bredow, T. Klüner and V. Staemmler, *J. Phys.: Condens. Matter*, 2004, **16**, S2497.
10 T. Klüner, H.-J. Freund, J. Freitag and V. Staemmler, *J. Chem. Phys.*, 1996, **104**, 10030.
11 B. O. Roos, *Adv. Chem. Phys.*, 1987, **69**, 399.
12 H.-J. Werner, *Adv. Chem. Phys.*, 1987, **69**, 1.
13 K. Andersson, P.-Å. Malmqvist, B. O. Roos, A. J. Sadlej and K. Wolinski, *J. Phys. Chem.*, 1990, **94**, 5483.
14 K. Andersson, P.-Å. Malmqvist and B. O. Roos, *J. Phys. Chem.*, 1992, **96**, 1218.

15 T. Klüner, S. Thiel, H.-J. Freund and V. Staemmler, *Chem. Phys. Lett*., 1998, **294**, 413.
16 G. Karlström, R. Lindh, P.-Å. Malmqvist, B. O. Roos, U. Ryde, V. Veryazov, P.-O. Widmark, M. Cossi, B. Schimmelpfennig, P. Neogrády and L. Seijo, *Comput. Mater. Sci*., 2003, **28**, 222.
17 U. Maier and V. Staemmler, *Theor. Chim. Acta*, 1989, **76**, 95.
18 V. Staemmler, *Theor. Chim. Acta*, 1977, **45**, 89.
19 R. Fink and V. Staemmler, *Theor. Chim. Acta*, 1993, **87**, 129.
20 J. Wasilewski, *Int. J. Quantum Chem*., 1989, **36**, 503.
21 R. Lindsay, P. Baumgärtel, R. Terborg, O. Schaff, A. M. Bradshaw and D. P. Woodruff, *Surf. Sci*., 1999, **425**, L401.
22 J. T. Hoeft, M. Kittel, M. Polcik, S. Bao, R. L. Toomes, J. H. Kang, D. P. Woodruff, M. Pascal and C. L. A. Lamont, *Phys. Rev. Lett*., 2001, **87**, 086101.
23 S. F. Boys and F. Bernardi, *Mol. Phys*., 1970, **19**, 553.
24 D. Kröner, I. Mehdaoui, H.-J. Freund and T. Klüner, *Chem. Phys. Lett*., 2005, **415**, 150–154.
25 R. Wichtendahl, M. Rodriguez-Rodrigo, U. Härtel, H. Kuhlenbeck and H.-J. Freund, *Surf. Sci*., 1999, **423**, 90.
26 P. R. Antoniewicz, *Phys. Rev. B*, 1980, **21**, 3811.
27 W. Press, S. Teukolsky, W. Vetterling and B. Flannery, *Numerical Recepies in Fortran: The Art of Scientific Computing*, Cambridge University Press, New York, 2nd edn, 1992.
28 M. D. Feit and J. A. Fleck, *J. Chem. Phys*., 1983, **78**, 301.
29 R. Kosloff, *J. Phys. Chem*., 1988, **92**, 2087.
30 R. Heather and H. Metiu, *J. Chem. Phys*., 1987, **86**, 5009.
31 J. W. Gadzuk, *Surf. Sci*., 1995, **342**, 345.
32 M. Menges, B. Baumeister, K. Al-Shamery, H.-J. Freund, C. Fischer and P. Andresen, *J. Chem. Phys*., 1994, **101**, 3318.
33 G. Eichhorn, M. Richter, K. Al-Shamery and H. Zacharias, *J. Chem. Phys*., 1999, **111**, 386.

 